A High-Precision Flat Field Method Based on Image Stitching for Short Wavelength Instruments

XingJun Gao[1,2] · Bo Chen[1] ⬤ · LingPing He[1] ·
Xin Zheng[1]

Abstract We present a method to obtain a large-scale flat field using only small offsets. The method is derived from the Kuhn, Lin, and Loranz (KLL) algorithm (*Publ. Astron. Soc. Pacific* **103**, 1097, 1991), but combined with the image stitching technique. Due to complementary images, which optimize and replace the bad edges, the accuracy is better than 0.1 root mean square across the full field of view, and the pixel-level relative error is also better than 0.1%. Another significant advantage is that its small sampling interval provides a rapid sampling time, while maintaining a large-scale and high-precision flat field (beyond 95% proportion). We have proved its high efficiency and robustness by simulating a cosine and a Gaussian CCD response and comparing the results with the KLL algorithm. Finally, a visible non-uniform target experiment with a uniform response was performed to prepare for the upcoming solar *X-ray Extreme Ultraviolet Imager* (X-EUVI) instrument on the *FengYun*-3 (FY-3) weather satellite series.

Keywords Calibration · Flat field · Image processing

1. Introduction

The solar *X-ray Extreme Ultraviolet Imager* (X-EUVI) is one of the important remote sensing instruments on the *FengYun*-3 (FY-3) satellite (satellite in Sun-synchronous orbit, total field of view of $42' \pm 2'$, observation range at 0.6 nm − 8 nm for channel 1 and 19.5 nm as central wavelength for channel 2) (Zhang *et al.*, 2019). Its mission is to use X-ray and extreme ultraviolet solar radiation to achieve a long-term, continuous, and high-time-resolution observation of the Sun, to obtain high-resolution images, and to provide a reference for accurate space weather prediction. When using high-resolution images of the Sun, it is important to be aware that significant uncertainties are caused by flat-fielding errors on the instru-

✉ B. Chen
Chen_bo_2019@163.com

1 Changchun Institute of Optics, Fine Mechanics and Physics, Chinese Academy of Sciences, Changchun, Jilin 130033, China

2 University of Chinese Academy of Sciences, Beijing 100049, China

ment itself. For example, for the *Solar and Heliospheric Observatory* (SOHO)/*Michelson Doppler Imager* (MDI) continuum images, the amplitude of the flat-fielding error has nearly doubled over the 11 years of instrument operation in 2008, which may cause systematic errors in all motion-tracking and most feature recognition algorithms (Potts and Diver, 2008, 2009). Therefore, like any other observation instrument of the Sun, we need a suitable flat field calibration method and a scheme.

Often the standard "flat-fielding" principle is to illuminate an image-array detector with a uniform light source and to measure the pixel-level difference in response. Astronomers use "dome" flats, "twilight" flats, or "night sky" flats to generate a uniform bright image (Mackay, 1986). However, the accuracy can be hardly better than the uniformity of the respective flat field (about 1%), since the optical configuration of the ray paths or the diffuser is not identical to the actual data-taken configuration of the system. Besides, the artificial uniform lighting target is normally a flat-plate diffuser or an integrating sphere (Heath *et al.*, 1993). Since its operating wavelength depends on the optic devices, and its precision is limited by the manufacturing technology, there is no available material in the X-EUVI wavelength to offer an artificial uniform target. Thus, none of these methods is appropriate for the X-EUVI or for real-time, on-orbit remote sensing observation in short wavelength.

Another way, not requiring a completely uniform target, uses only a series of spatially displaced images. It is convenient to work out a response distribution of the image plane, as long as we know exactly the displacement of each shifted image. Kuhn, Lin, and Loranz developed this algorithm initially for calibrating the spatial non-uniformity of image-array (CCD-type) detectors (Kuhn, Lin, and Loranz, 1991, KLL hereafter), which were motivated by astronomical CCD applications. Then, Toussaint, Harvey, and Toussaint applied the over-relaxation algorithm to KLL's method simultaneously, which enhances the convergence (Toussaint, Harvey, and Toussaint, 2003). Chae proposed a more practical method to search for the flat pattern, the object image, the light level, and optionally the relative displacements at the same time (Chae, 2004). However, the accuracy may be lower than KLL's method. Different from the KLL's algorithm based on the minimum of the sum of the squared errors (SSE), Xu *et al.* applied a new concept called the maximum correntropy criterion (MCC) to get a higher accuracy. The computing time is shorter but the procedure is much more complex (Xu *et al.*, 2016).

On one side, although these approaches increase the accuracy of the image plane or enhance convergence of the algorithm, none of them modifies the sharp drop-off near the corners caused by the internal vignetting or the limitation of the algorithm (Scherrer *et al.*, 1995; Boerner *et al.*, 2012). Optimization of the edge is vital to raise the precision across the full field of view. On the other side, the solar image can be shifted in two ways, moving the spacecraft is rather slow on time scale, while PZT (piezo-electric transductors) can only provide a small spatial offset (Wachter and Schou, 2009; Hoeksema *et al.*, 2018). At the account of these points, we need a method to obtain a large-scale and high-precision flat field only using small offsets. So we focus on incorporating image registration and fusion techniques into the subsequent computational analysis, which depends on the accuracy of the compensation image and the process of seamless stitching (Zitová and Flusser, 2003).

Compared with feature-based matching technology, contour recognition, region-based matching technology is easier and more efficient (Li *et al.*, 1995). In addition, to eliminate the seams, we choose a weighted smoothing method, which is more precise than the median filtering and easier to achieve than the wavelet transform (Le Moigne, Campbell, and Cromp, 2002) or classic algorithm of mosaics (Burt and Adelson, 1983) at the same accuracy level. This method is flexible and accurate, and can be applied to real-time, on-orbit remote sensing observation or X-ray extreme ultraviolet applications in vacuum, especially for our solar X-EUVI instrument.

The article is structured as follows. Section 2 introduces the KLL's basic algorithm (Section 2.1) and our improvement principles based on digital image processing (Section 2.2). Section 3 proves the feasibility of the algorithm by establishing simulation models. Section 4 describes the experiments to verify this method and analyzes the results. Section 5 discusses the conclusions of the study.

2. Derivation of the Method

2.1. KLL Algorithm

After being corrected by the null input response and amplifier bias, and assuming that the intensity of the object is stable and invariant when we take a series of shifted image samples, the image-array detector can be considered as a system whose response is independent of the input intensity of the object, but depends on the optical sensitivity differences of each pixel element, as follows:

$$r(x) = o \cdot f(x). \tag{1}$$

In this equation, r and o are the actual inhomogeneous response and intensity of the object, respectively, and f is the gain at a fixed position x.

Let $R(x) \equiv \ln(r(x))$ and $F(x) \equiv \ln(f(x))$. The relationship between the gray value and response of each pixel in two images is given as Equation 2, where the displacements are described by a_i and a_j,

$$R_i(x + a_i) - R_j(x + a_j) - F_i(x + a_i) + F_j(x + a_j) = 0. \tag{2}$$

We can calculate a least-squares solution for the distribution of the gain if we build an over-sampled and over-determined linear equation set about $r(x)$:

$$\sum_{i<j,x} \left[R_i(x + a_i) - R_j(x + a_j) - F_i(x + a_i) + F_j(x + a_j) \right]^2 = 0. \tag{3}$$

Differentiating Equation 3 with respect to $F(x)$, and setting the initial solution $F^0(x) = 0$, we arrive at an iterative solution:

$$F^{t+1}(x) = K(x) + \frac{1}{n(x)} \sum_{i<j} \left[F^t(x - a_i + a_j) - F^t(x - a_j + a_i) \right], \tag{4}$$

where

$$K(x) = \frac{1}{n(x)} \sum_{i<j} \left[R_i(x) - R_j(x - a_i + a_j) \right] + \left[R_j(x) - R_i(x - a_j + a_i) \right]. \tag{5}$$

This is the form of a solution to Poisson's equation, $n(x)$ counts the number of bracketed operations that contribute to the sum. This model is useful where other models fail, especially when we cannot offer a proper uniform target in short wavelength instruments. Yet, the limitation is that its accuracy near the corner is too low to be accepted because internal vignetting weakens the light intensity from the center to the surrounding. Judged by the auto-correlation boundary extraction process, only pixels inside the boundary will be calculated. That is why we propose our method.

The approximate optimal solution of this least-squares method is not unique. In order to avoid contingency and to improve credibility, the calibration result takes the average of multiple sets of data.

2.2. Improved Algorithm

Due to internal vignetting and the algorithm itself, the KLL model is limited at the sharp edges around the four corners, and the accuracy outside the boundary is low. To improve the accuracy near the corners, we adapt image registration and fusion techniques. The most difficult thing is to cope with the overlapping parts of the image.

For a flat-fielding image, there are generally no feature points, unless the image plane is contaminated. So boundary extraction or complex image registration and fusion techniques based on features are worthless. Our method is based on pixel grayscale correlation, using the gray value to reflect all the information of the recorded image. The measure of similarity used for region-based registration is a normalized cross-correlation (correlation coefficient), as defined by the following equation:

$$\gamma(x, y) = \frac{\sum_{s,t}[w(s, t) - \bar{w}][f(x + s, y + t) - \bar{f}_{xy}]}{\sqrt{\sum_{s,t}[w(s, t) - \bar{w}]^2 \sum_{s,t}[f(x + s, y + t) - \bar{f}_{xy}]^2}}, \tag{6}$$

where w is a template, $\overline{w}$ the average value of the template elements calculated only once, f the image, $\overline{f}_{xy}$ the average for the coverage area of w and f, and where the summation is performed in the coverage area by s and t, (x, y) is a coordinate pair. The higher the absolute value $|\gamma(x, y)|$ is, the better the match will. The steps of the method are as follows:

i) Extract a region of interest (ROI).

For a flat-fielding image from the KLL model, we need to extract a ROI as a mask waiting for image stitching. The pixels within this mask remain unchanged, while the pixels outside will be replaced and optimized by complementary images.

Often an obvious boundary can be identified directly and positioned, but when it cannot be detected, it is necessary to introduce a threshold, T, to filter out the low-precision areas. This mask protects the high-precision portion of the raw data and the special spots produced by the pollution.

ii) Get complementary images.

We make full use of the high precision of sampling center, which is moved to the sharp drop-off edges. For the solar X-EUVI, there are two systems to control the shift, one is to shift the imager through a 2D tracking turntable, the other is a precision control system with PZT. So far, this scheme not only greatly saves the total sampling time, but also obtains a maximum field of view range with relatively small offsets.

iii) Image stitching.

When stitching the mask and the complementary images, the most essential step is to eliminate the stitching seams. In practice, a weighted smoothing approach is still chosen based on pixel grayscale correlation. The gray value f of each pixel at the stitched image is obtained by the weighted average of the corresponding points in image f_1 and f_2.

$$f = \frac{\sum_{x,y \subset f_1} f_1(x, y)}{n_1} + k \frac{\sum_{x,y \subset f_2} f_2(x, y)}{n_2}, \tag{7}$$
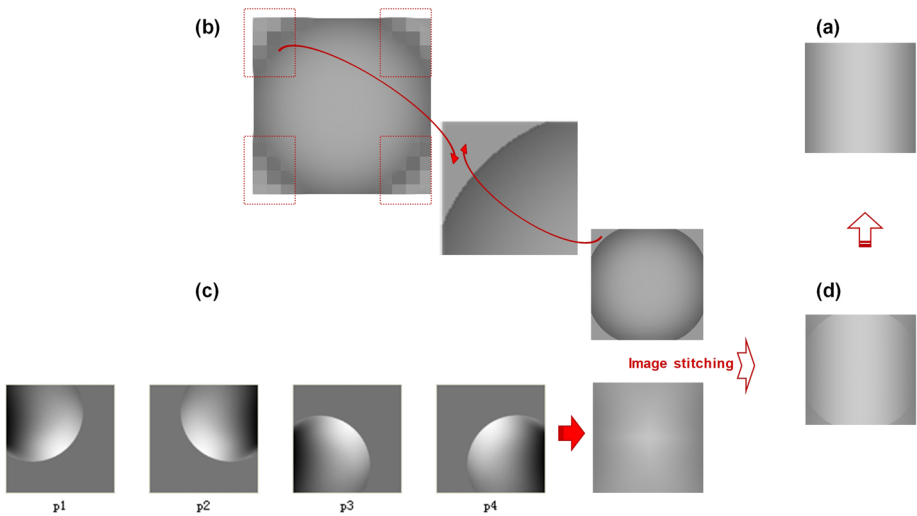
Figure 1 (**a**) Simulated ture CCD gain variation. (**b**) The initial result of KLL with sharp drop-off. (**c**) The complementary images and combination thereof. (**d**) The final result of the new method.

where k is the weighting factor, and n_1 and n_2 are the number of valid pixels in the two stitched images.

3. Results for Simulated Data

We tested the new method by simulating two sets of data. When the ideal response distribution of the CCD was assumed to be a cosine function, the initial result of the KLL algorithm is shown in Figure 1. Kuhn *et al.* have already explained how its solution depends on the signal-to-noise ratio, the number of pixels, the number of image displacements, and the number of iterations. Our idea was to incorporate image processing technology, which means that the complementary images were critical to get a large-scale and high-precision flat field. We chose the pixel-to-pixel relative error, ω, and its proportion to reflect the accuracy, and the RMS of each line, σ, as the evaluation criteria:

$$\omega = \left| \frac{F(x) - F_{\text{ture}}(x)}{F(x)} 100\% \right|, \tag{8}$$

$$\sigma = \sqrt{\sum_{n=1}^{N} \frac{(\omega(n) - \overline{\omega})^2}{N}}, \tag{9}$$

where $F_{\text{ture}}(x)$ is the actual flat-fielding response, $F(x)$ is the calculated result, n is the number of the line, and N is the number of pixels in each line.

To work out a large-scale and high-precision flat field for the coming solar X-EUVI instrument, our flow chart of the new method is shown in Figure 2. The stitching steps were indicated in Section 2.2. It should be pointed out that the algorithm we had implemented does not interpolate to sub-pixel resolution so that the real data must be oversampled. The extraction method of the ROI was not unique. Different gain variation for different CCDs
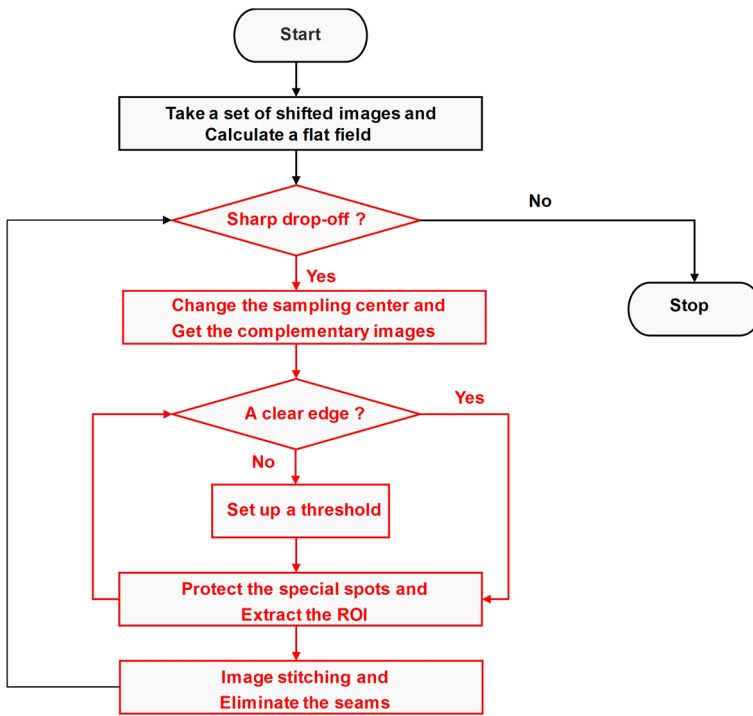
Figure 2 Flow chart of the improved algorithm with an explicit strategy (in *red color*) to solve the sharp drop-off problem.

and different pollution conditions may require a different boundary extraction method, setting a threshold is just the most basic step.

After setting the parameters: number of sampling $P = 121$, number of iterations $i = 50$, and threshold $T = 0.01$ or 0.05, the resulting 3-D view relative error, ω, its 2D view, and RMS, σ, are shown in Figure 3. Clearly, the results of the KLL's algorithm have large boundary errors and high intermediate precision. For a sinusoidal distribution image plane, the proportion of $\omega < 0.01\%$ was just 82.72%, the maximum of it was up to 0.2%, and the maximum of its RMS, σ, was almost 0.07. Moreover, for a Gaussian distribution image plane, the proportion of $\omega < 0.05\%$ was about 88.27%, the maximum of it was over 0.22%, and the σ was near 0.12. There were obvious flaws in the four dead corners, so it was imperative to improve its performance.

One indispensable step was to obtain the complementary images for the boundary. We obtained the complementary part by adjusting the sampling center to the worst position, as shown in Figure 1c. Then the image stitching process is shown in Figure 2 (in red). In Figure 4, the stitching results of the combination with the complementary images are shown. The maximum of ω and σ were much lower than the initial results, while the proportion of $\omega < 0.01\%$ or $\omega < 0.05\%$ was also much lower. So we had to combine the advantages of these two results to get the best high-precision flat field.

Another critical step was to eliminate the stitching seams. The results of the stitching combination image dramatically improved the accuracy of the boundary, but the effect in the middle was poor. So after denoising, the ROI of the initial data with high precision in the middle was extracted into a mask. We opted for a weighted smoothing approach to
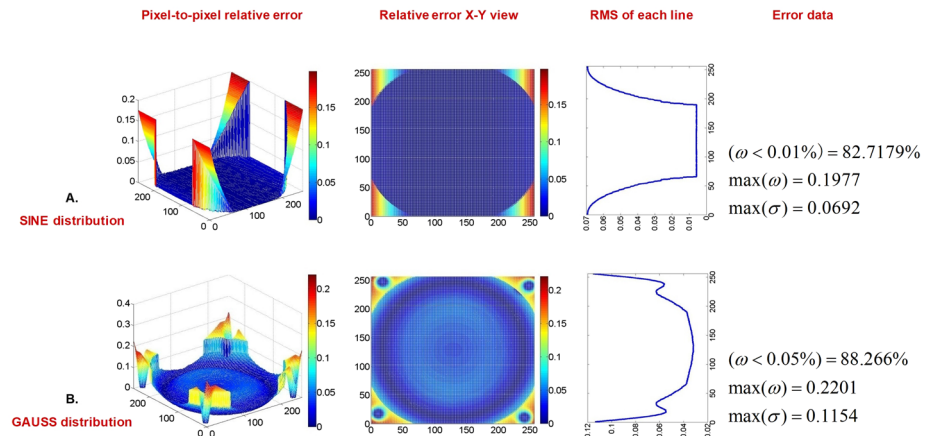
Figure 3 Initial results of the KLL's algorithm for two image planes.
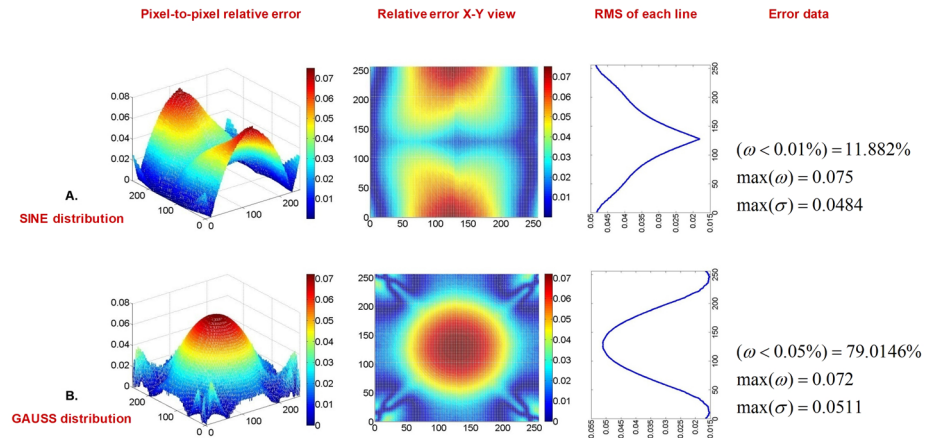
Figure 4 Results of the combination of complementary images for two image planes.

implement image registration fusion. The red line in Figure 5 shows the final results, the maximum of ω and σ went down to a lower level than the initial data, and the proportion of $\omega < 0.05\%$ was completely 100%. So we could provide a high-precision flat field with an accuracy better than 0.05%.

4. Results for Experimental Data

We have done experiments with a non-uniform visible target, as an approach to the X-EUVI data, because the real data from the experiment could not have the ideal characteristics of the simulated data. The flat-fielding experiments for a MQ042CG-CM CMOS with 500 × 500 pixels (ximea xiQ series) was completed in two steps. One was done at system-level (experiment A) and the other at component-level (experiment B). The masks of these two experiments are shown in Figure 6.
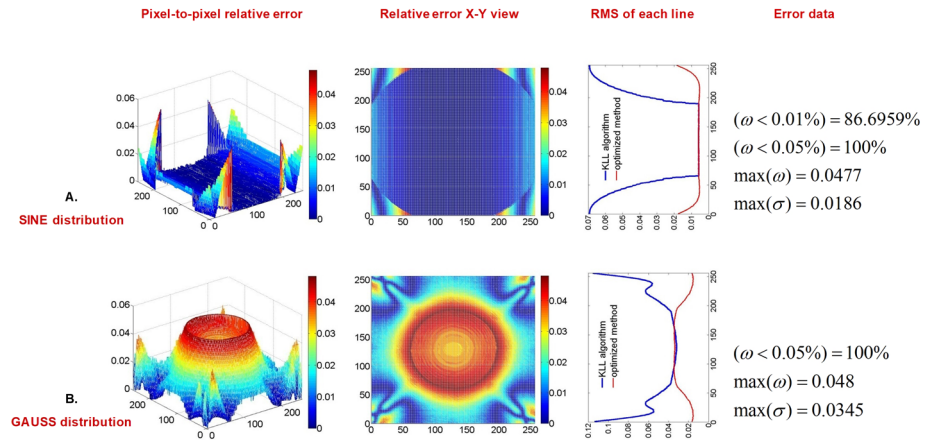
Figure 5 Final results of the optimized method for two image planes. *Blue line* for the KLL algorithm, *red line* for the optimized method.
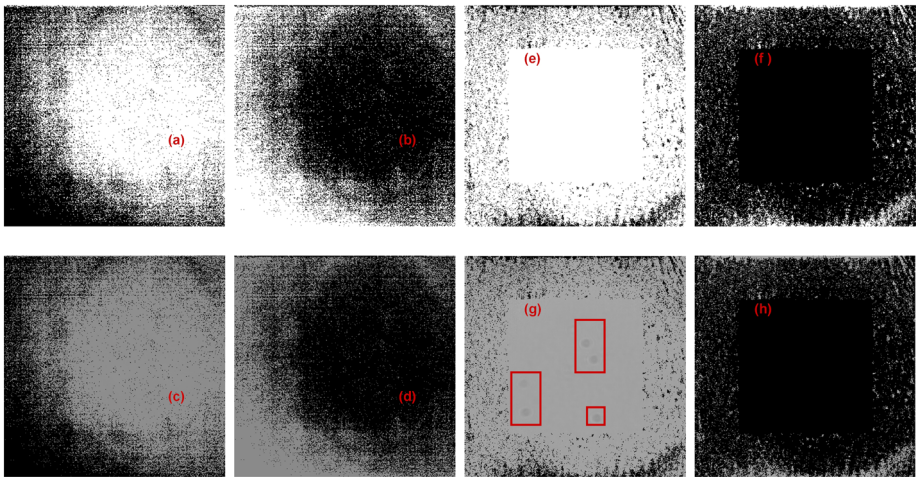
Figure 6 Masks of experiments. (**a**), (**b**), (**c**), and (**d**) correspond to a system-level flat field. (**e**), (**f**), (**g**), and (**h**) correspond to a component-level flat field. (**a**) − (**b**) and (**e**) − (**f**) are mask pairs, while (**c**) − (**d**) and (**g**) − (**h**) are pairs waiting for weighted stitching. The *red rectangles* mark the special spots.

The system-level flat field calibration was fitted with an imaging lens as an imaging system. According to the traditional "night sky" flats, we used this system to photograph the quiet night and early morning sky, and selected a result with good uniformity as a reference to normalize the results from the KLL algorithm and from our optimized algorithm. A flat field merely represents the response efficiency of an image plane by grayscale, so that it is not limited by a maximum, a minimum, or an internal range. The normalization is just for comparison and for attesting the correctness of our method. We had run some sets of cases, and found that nine-image model was the best result of the KLL algorithm. Table 1 shows the effect of different sample numbers on the accuracy.

Table 1 Effect of different sample numbers, P, on the method accuracy.

	P=9	P=25	P=27	P=45	P=81
$\omega < 0.01(\%)$	66.0472	45.2296	41.7668	41.1336	34.6444
$\max(\omega)$	0.0418	0.0454	0.0457	0.0454	0.0461
$\max(\sigma)$	0.0212	0.0231	0.0225	0.0237	0.0239
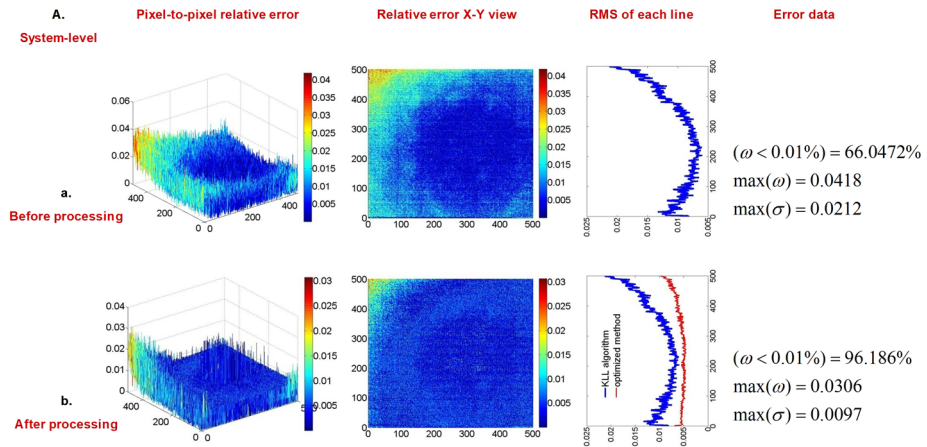
Figure 7 Results of system-level flat field. *Blue line* for the KLL algorithm, *red line* for our optimized method.

The results obtained with the KLL algorithm are shown in Figure 7a. The proportion of $\omega < 0.01\%$ was merely 66.05%. The maximum of σ was not good enough. After image processing, as shown in Figure 7b, the proportion of $\omega < 0.01\%$ was raised to 96.19%, also the maximum of σ was reduced to an acceptable value, which indicates that this new technique was much better than the traditional method. Figure 8 shows the real data.

Unlike a simulated CCD image plane, the sensitivity differences of a real CMOS are uneven, as shown in Figure 8h. We treated these spots as special spots in the post-processing, when we carried out a component-level flat field calibration without any imaging system, just to test the performance of the COMS. The number of iterations was selected according to a set of number tests (see Table 2), 15 iterations proved to be easy to use.

In general, the result of the KLL algorithm was pretty good (see Figure 9a). The proportion of $\omega < 0.01\%$ was about 84.56%. Nevertheless, we improved it to 94.43% after optimizing, and for a 3-D view panel b was much clearer than panel a. σ was optimized from 0.0316 down to 0.0145 as well. The prominent parts brought from spots might be the largest system error due to the obvious non-linearity. The algorithm would modulate some temporal changes into false spatial gain variations if the source was not as stable as an ideal one, but it cannot deal with the dust in the protection mirror of the CMOS. The advantage is that this feature could be applied to find pollution changes of the mirror by performing the two experiments.
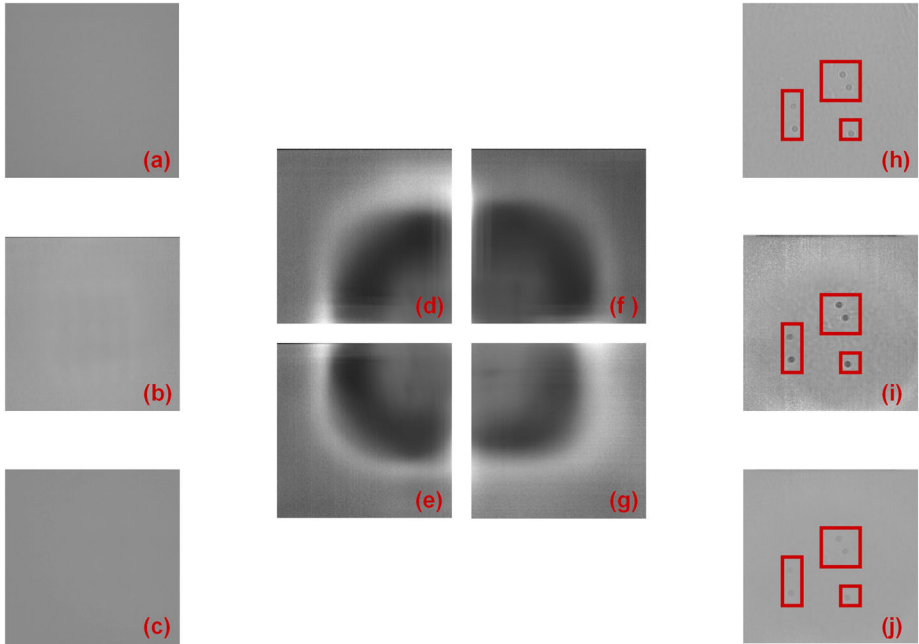
Figure 8 (**a**), (**b**), and (**c**) correspond to an ideal CCD, KLL's result, and an optimized result for experiment A, respectively. (**d**), (**e**), (**f**), and (**g**) are complementary parts of the system-level experiment. (**h**), (**i**), and (**j**) correspond to an ideal CCD, KLL's result, and an optimized result for experiment B, respectively. The *red rectangles* mark the special spots.
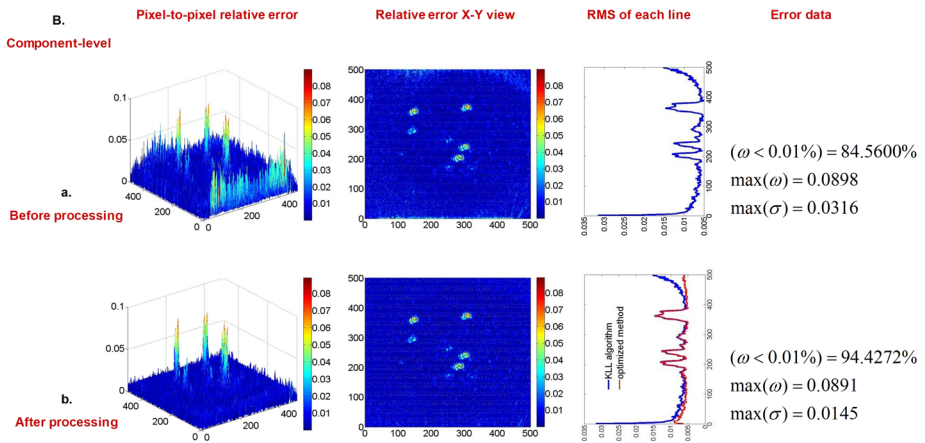
Figure 9 Results of component-level flat field. *Blue line* for the KLL algorithm, *red line* for our optimized method.

5. Conclusion

The algorithm we introduced is based on the assumption that the light source is stable during the sampling period. The simulation case does not change, while the time-stability of

Table 2 Effect of different iteration times, i, on the method accuracy.

	i=5	i=10	i=15	i=20	i=30	i=40	P=50
$\omega < 0.01$(%)	84.1812	84.5600	84.7968	84.7792	84.6528	84.5376	84.4836
$\max(\omega)$	0.0904	0.0898	0.0898	0.0886	0.0880	0.0880	0.0880
$\max(\sigma)$	0.0322	0.0316	0.0312	0.0312	0.0312	0.0312	0.0312

the white light experiment is about 1%, which should not impact the accuracy excessively. According to the experiment, the parameters can be preset as: number of sampling $P = 9$, number of iterations $i = 15$, the threshold is defined by the user. However, in the case of high contrast, the parameters might have to be optimized to refer to the real situation.

The method is advantageous as it is not influenced by the working wavelength, manufacturing technology, or even uniformity of the target. Especially, its large-scale flat field using only small offsets, which provides a rapid working time, while the accuracy is lower than 0.1 RMS across the full field of view, and the pixel-level relative error is also better than 0.1%. The disadvantage is that the complementary images entirely depend on whether the sampling center can be moved to the position to be improved.

In summary, our method can substantially increase the quality of a flat field. It is not restricted to the X-EUVI mission and can be useful for other solar observation instruments.

Disclosure of Potential Conflicts of Interest   The authors declare that there are no conflicts of interest.

Publisher's Note   Springer Nature remains neutral with regard to jurisdictional claims in published maps and institutional affiliations.

References

Boerner, P., Edwards, C., Lemen, J., Rausch, A., Schrijver, C., Shine, R., Shing, L., Stern, R., Tarbell, T., Title, A., Wolfson, C.J., Soufli, R., Spiller, E., Gullikson, E., McKenzie, D., Windt, D., Golub, L., Podgorski, W., Testa, P., Weber, M.: 2012, Initial calibration of the Atmospheric Imaging Assembly (AIA) on the Solar Dynamics Observatory (SDO). *Solar Phys.* **275**, 41. DOI. ADS.

Burt, P.J., Adelson, E.H.: 1983, A multiresolution spline with application to image mosaics. *ACM Trans. Graph.* **2**, 217.

Chae, J.: 2004, Flat-fielding of solar magnetograph observations using relatively shifted images. *Solar Phys.* **221**(1), 15.

Heath, D.F., Wei, Z., Fowler, W.K., Nelson, V.W.: 1993, Comparison of spectral radiance calibrations of SBUV-2 satellite ozone monitoring instruments using integrating sphere and flat-plate diffuser techniques. *Metrologia* **30**(4), 259.

Hoeksema, J.T., Baldner, C.S., Bush, R.I., Schou, J., Scherrer, P.H.: 2018, On-orbit performance of the helioseismic and magnetic imager instrument onboard the Solar Dynamics Observatory. *Solar Phys.* **293**, 45. DOI. ADS.

Kuhn, J.R., Lin, H., Loranz, D.: 1991, Gain calibrating nonuniform image-array data using only the image data. *Publ. Astron. Soc. Pacific* **103**(668), 1097.

Le Moigne, J., Campbell, W.J., Cromp, R.F.: 2002, An automated parallel image registration technique based on the correlation of wavelet features. *IEEE Trans. Geosci. Remote Sens.* **40**, 1849. DOI. ADS.

Li, H., Member, S., Manjunath, B.S., Mitra, S.K.: 1995, A contour-based approach to multisensor image registration. *IEEE Trans. Image Process.* **4**, 320.

Mackay, C.D.: 1986, Charge-coupled devices in astronomy. *Annu. Rev. Astron. Astrophys.* **24**(1), 255.

Potts, H.E., Diver, D.A.: 2008, Post-hoc derivation of SOHO Michelson doppler imager flat fields. *Astron. Astrophys.* **492**, 863. DOI.

Potts, H.E., Diver, D.A.: 2009, A repository of precision flat fields for high-resolution MDI continuum data. *Solar Phys.* **258**(2), 343.

Scherrer, P.H., Bogart, R.S., Bush, R.I., Hoeksema, J.T., Kosovichev, A.G., Schou, J., Rosenberg, W., Springer, L., Tarbell, T.D., Title, A., Wolfson, C.J., Zayer, I., MDI Engineering Team: 1995, The Solar Oscillations Investigation – Michelson Doppler Imager. *Solar Phys.* **162**, 129. DOI. ADS.

Schou, J., Scherrer, P.H., Bush, R.I., Wachter, R., Couvidat, S., Rabello-Soares, M.C., Bogart, R.S., Hoeksema, J.T., Liu, Y., Duvall, T.L., Akin, D.J., Allard, B.A., Miles, J.W., Rairden, R., Shine, R.A., Tarbell, T.D., Title, A.M., Wolfson, C.J., Elmore, D.F., Norton, A.A., Tomczyk, S.: 2012, Design and ground calibration of the Helioseismic and Magnetic Imager (HMI) instrument on the Solar Dynamics Observatory (SDO). *Solar Phys.* **275**, 229. DOI. ADS.

Toussaint, R.M., Harvey, J.W., Toussaint, D.: 2003, Improved convergence for CCD gain calibration using simultaneous-overrelaxation techniques. *Astron. J.* **126**(2), 1112.

Wachter, R., Schou, J.: 2009, Inferring small-scale flatfields from solar rotation. *Solar Phys.* **258**, 331. DOI. ADS.

Xu, G.-G., Zheng, S., Lin, G.-H., Wang, X.-F.: 2016, Flat-fielding of solar Hα observations based on the maximum correntropy criterion. *Astrophys. J.* **827**, 137. DOI. ADS.

Zhang, X., Chen, B., He, F., Song, K., He, L., Liu, S., Guo, Q., Li, J., Wang, X., Zhang, H.M., *et al.*: 2019, Wide-field auroral imager onboard the Fengyun satellite. *Light Sci. Appl.* **8**(1), 47.

Zitová, B., Flusser, J.: 2003, Image registration methods: A survey. *Image Vis. Comput.* **21**, 977. DOI.